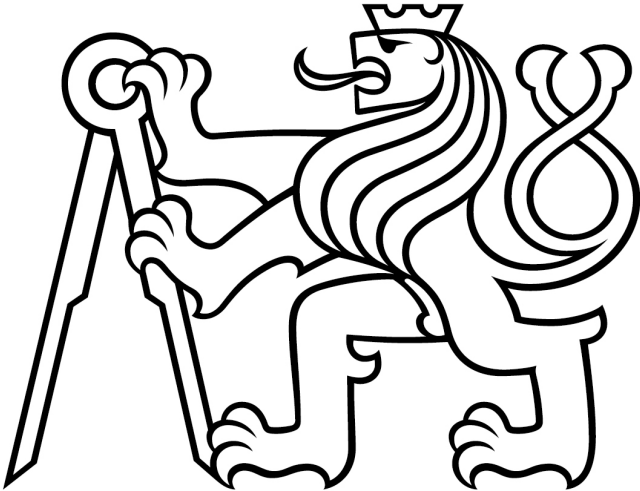


CZECH TECHNICAL UNIVERSITY IN PRAGUE



Doctoral Thesis Statement



Czech Technical University in Prague  
Faculty of Biomedical Engineering  
Department of Natural Sciences

LUCIE DUBOVSKÁ

**ESSENTIAL ELEMENTS TOWARDS THE  
DEVELOPMENT OF DIAMOND-BASED  
BIOSENSORS FOR BACTERIA DETECTION IN  
WATER**

Ph.D. Programme: *Biomedical and Clinical Technology*  
Branch of Study: *Biomedical and Clinical Technology*

Doctoral thesis statement for obtaining the academic title "Doctor of  
Philosophy" abbreviated to "Ph.D."

Kladno, October 2023

The Doctoral thesis was produced in combined Ph.D. study at the Department of Natural Sciences of the Faculty of Biomedical Engineering of the Czech Technical University in Prague.

**Candidate:** Ing. Lucie Dubovská  
Faculty of Biomedical Engineering, CTU in Prague  
nám. Sítná 3105, 272 01 Kladno, Czech Republic

**Supervisor:** Dr. Vincent Mortet, Ph.D.  
Institute of Physics, Czech Academy of Sciences  
Na Slovance 1999/2, 182 00 Prague 8, Czech Republic

**Co-Supervisor:** Prof. Abdelkrim Talbi, Ph.D.  
Institute of Electronics, Microelectronics and Nanotechnology  
Cité Scientifique, Avenue Henri Poincaré CS 60069  
59 652 Villeneuve d'Ascq Cedex, France

**Opponents:** .....  
.....  
.....

The doctoral thesis statements were distributed on: .....

The defence of the Doctoral thesis will be held on ..... at .....  
in front of the Board for the Defence of the Doctoral Thesis in the Doctoral programme Biomedical and Clinical Technology in the room No. .... of the Faculty of Biomedical Engineering of the CTU. Those interested may get acquainted with the Doctoral thesis at the Dean's Office of the Faculty of Biomedical Engineering of the CTU in Prague, nám. Sítná 3105, 272 01 Kladno, Czech Republic.

.....  
prof. Ing. Karel Roubík, Ph.D.  
Chairperson of the Board for the Defence of the Doctoral Thesis  
Faculty of Biomedical Engineering of the CTU in Prague  
nám. Sítná 3105, 272 01 Kladno, Czech Republic

# Contents

<b>1</b>	<b>Introduction</b>	<b>1</b>
<b>2</b>	<b>Aims of the Thesis</b>	<b>3</b>
<b>3</b>	<b>Methods</b>	<b>4</b>
3.1	Theoretical simulations . . . . .	4
3.2	SAW device fabrication & characterization . . . . .	5
3.3	Diamond layers deposition & characterization . . . . .	8
<b>4</b>	<b>Results</b>	<b>11</b>
4.1	FEM simulations of the properties of diamond coated LW-SAW sensors . . . . .	11
4.2	LW-SAW devices with continuous and discrete NCD coatings . . . . .	15
4.3	Enhancing the sensitivity of SAW sensors using the diamond surface phononic metamaterials . . . . .	19
4.4	Experimental investigation of the properties of diamond coated LW-SAW sensors . . . . .	23
4.5	Bacteriophage's tail fibers production . . . . .	31
4.6	Functionalization of the diamond layers . . . . .	35
4.7	BDD-coated QCM sensors for biosensing . . . . .	39
<b>5</b>	<b>List of publications</b>	<b>43</b>
<b>6</b>	<b>Summary</b>	<b>47</b>
<b>7</b>	<b>Resumé</b>	<b>48</b>

# 1 | Introduction

Detection and identification of pathogens is an important goal in food safety, medicine, public health or national security. Rapid detection of pathogens in medical samples can mean the difference between life and death of patients. Pathogen detection in food, water or air samples is an important part to maintain public health [1, 2]. It is estimated, that about 15 % of total mortality in the world is caused by infectious diseases. It became even bigger problem with change of the modern lifestyle, when the spread of the disease around the world is accelerated. [3] Bioterrorism is also huge concern, as food and water can be an excellent carrier of the pathogenic bacteria [4]. Each of us has experienced the need for fast, inexpensive and selective pathogen detection method, when we came through the global pandemic of the disease COVID-19 in recent years and this pandemic paralyzed the world and greatly affected our lives.

Water-borne diseases are caused mainly by viruses, fungi, bacteria and protozoan parasites [5]. *Escherichia coli*, *Salmonella typhimurium*, *Campylobacter jejuni*, *Legionella pneumonia* or *Staphylococcus aureus* are few bacteria strains, that can cause serious health problems. Among them, *E. coli* is reported to cause large scale life lost [6]. *E. coli* O157:H7 strains produce Shiga toxins, that can cause stomach pain, diarrhea, inflammation or even extreme instances like hemorrhagic enteritis and hemolysis, mainly found in babies and young children. Quality water monitoring is based on the testing of presence of *E. coli* cells, as it is still the best indicator of fecal contamination. According to WHO, water is considered as intermediate risk, when it contains only 10 to 100 viable *E. coli* cells per ml [7].

Detection method for water quality monitoring should be quick, sensitive, selective and ideally real-time. As conventional detection methods are time-consuming and labor intensive, researchers are focusing on the development of biosensing methods. In general, biosensors

---

should be inexpensive, easy to operate, label-free with minimal sample processing, selective with the ability to distinguish between bacteria serotypes. The key requirement for close-to-real-time monitoring is the stability of the bioreceptor [1, 6].

In this Thesis, we propose the use of Love wave-SAW biosensor with integrated CVD layer as an interface for the attachment of bacteriophage's tail fibers as bioreceptor for the bacteria detection in water. LW-SAW sensors can monitor cells behavior in liquids in the simple and non-invasive way with avoiding contact of the liquid with electrodes, and they are a promising probing method in biology and biomedical research. The proposed structure should also fulfill the requirements stated above. Acoustic wave devices are easy to fabricate and the use of Love waves allows sensing in liquids. Additionally, Love wave surface acoustic wave sensors possess the highest sensitivity among acoustic sensors [8]. Diamond has advantageous good chemical inertness together with multiple various surface functionalization possibilities. Reported prolonged stability of attached biomolecules is important to ensure close-to-real-time monitoring [9–11]. The specificity of the sensor is addressed by the functionalization of the diamond surface using bacteriophage's tail fibers.

## 2 | Aims of the Thesis

This work aims to carry out essential research on diamond-coated LW-SAW sensors to determine their suitability for pathogenic bacteria detection in aqueous solutions.

The research directions are more particularly specified as follows:

1. Theoretical investigation of diamond-coated LW-SAW sensors
  - To study the effect of different materials on the properties of diamond-coated LW-SAW sensors, such as phase velocity, electromechanical coupling coefficient and sensitivity
  - To discuss the possibilities to obtain high sensitive LW-SAW sensor with diamond coating
2. Fabrication and characterization of diamond coated LW-SAW sensors
  - To fabricate LW-SAW sensors, study its properties and evaluate the accuracy of theoretical results
  - To fabricate LW-SAW sensors with different types of diamond coatings and discuss their properties
3. Functionalization of diamond surface
  - To produce N-terminated His-tagged bacteriophage's tail fibers and study their binding to the bacterial host cells
  - To attach produced tail fibers to the diamond surface

# 3 | Methods

## 3.1 Theoretical simulations

### Basic model

Theoretical simulations were carried out using finite element method in COMSOL Multiphysics software. A basic unit cell model consists of 60  $\mu\text{m}$ -height piezoelectric substrate (quartz,  $\text{LiNbO}_3$ ,  $\text{LiTaO}_3$ ) covered by a guiding layer. Floquet periodic conditions were applied along the  $y$ -axis and  $x$ -axis to obtain whole crystal by repetition of the unit cell. The piezoelectric substrate was divided into two parts, the lower part was responsible for wave damping and the bottom of piezoelectric substrate was kept fixed to suppress wave reflections.

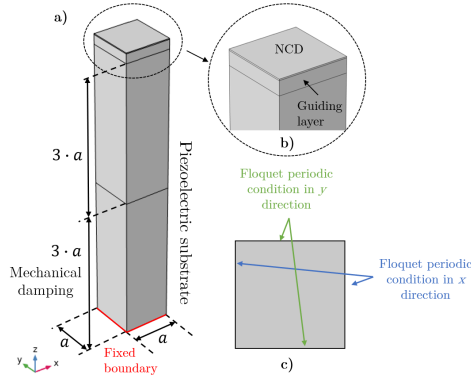


Figure 3.1: Basic COMSOL model used for theoretical calculations: a) whole structure, b) detail of the upper part with the guiding and diamond layers c) top view with shown periodic conditions

### Phononic crystal model

A 30  $\mu\text{m}$ -height 90ST-cut quartz substrate generating fast shear (SH) waves that propagates along the  $x$ -axis was used. To calculate the dispersion curves of the band structure, unit cell of the PnMs with the square array period with lattice constant  $a$ , was constructed. The irreducible Brillouin zone (BZ) was square bounded by  $\Gamma$ -X-M-Y- $\Gamma$  and the band structures were calculated only in the  $\Gamma$ -X direction. The model setup was then the same as described in previous section.

### Transmission spectra model

The simulation was realized by using the SAW device model consisting of two parts of IDTs and PnC located between the IDTs electrodes. As the model was symmetrical along the  $y$ -axis, the boundary periodic conditions were applied to the  $y$ -axis reducing the model to only one period. To avoid undesired reflections, the model was surrounded by perfectly matched layer and lateral and bottom sides were kept fixed. To obtain the fast shear acoustic waves, 20 pairs of 200 nm thick IDTs aluminum electrodes were added on top of the piezoelectric 90ST-cut quartz substrate. To excite the acoustic waves in the quartz substrates, the harmonic voltage  $V_0 = 1$  V was applied on the even fingers of the IDTs acting as a transmitter. Odd fingers were grounded. Generated acoustic waves confined in the  $\text{SiO}_2$  guiding layer propagated through the phononic crystals, consisted of 10 pillars, to the second set of IDTs fingers acting as a receiver. The output signal was obtained by averaging voltage variations between the even and odd IDTs fingers, where odd fingers were grounded and even fingers were set to zero surface charge accumulation.

## 3.2 SAW device fabrication & characterization

LW-SAW sensors were fabricated using conventional microtechnology techniques at Institute of Physics CAS and at CEITEC (Central European Institute of Technology) in cooperation with Ing. Imrich Gablech,

Ph.D. Schematic of the fabrication process is shown in the figure 3.2.

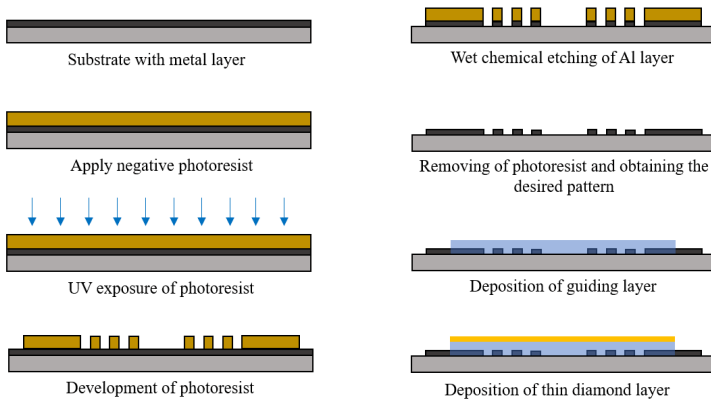


Figure 3.2: Scheme of a process for patterning IDT electrodes followed by guiding and diamond layer deposition

### SAW device fabrication at IoP

Prior to aluminum metal deposition, piezoelectric substrates were cleaned by sonication in acetone, isopropyl alcohol and hot deionized water for 5 minutes each followed by cleaning in mixture of sulfuric acid  $\text{H}_2\text{SO}_4$  (98%) and hydrogen peroxide (30%) (mixture ratio 1:1) for 10 minutes and rinsed 5x in the deionized water. 200 nm thick aluminum layers were deposited by a sputtering method (0.5 Pa, 16 sccm Ar, 420 W, 450 V with target diameter 100 mm).

Interdigital transducers (IDTs) electrodes were patterned using optical photolithography technique followed by chemical wet etching. Negative photoresist ma-N 1410 (Micro resist technology GmbH) was deposited on metal coated piezoelectric substrates by spin coating (3000 rpm, 30 s) followed by baking (110 °C, 150 s) on a hot plate. Exposure of photoresist was done using laser writing MicroWriter (Durham) apparatus followed by hard baking (120 °C, 150 s). The exposed pattern was developed in ready-to-use developer ma-D 533/S (Micro resist

technology GmbH) for 40 s and thoroughly rinsed in deionized water and dried using the cleaned and dry compressed air. The final pattern was obtained by wet chemical etching of aluminum layer in the mixture of  $\text{H}_3\text{PO}_4$  :  $\text{CH}_3\text{COOH}$  :  $\text{HNO}_3$  :  $\text{H}_2\text{O}$  with the mixing ratio 19:1:1:2 for 4 minutes. Then the samples were rinsed in isopropyl alcohol and DI water before being dried using cleaned and dry compressed air.

Amorphous  $\text{SiO}_2$  layers were deposited at IoP by RF magnetron sputtering method or at IEMN, Lille, France using low temperature PECVD Plasmalab 80 plus deposition system (Oxford Instruments). Used conditions are reported in table 3.1. IDTs pads were mechanically protected during all the depositions.

 Table 3.1: Amorphous  $\text{SiO}_2$  layers deposition conditions

	$\text{SiO}_2$ (IEMN)	$\text{SiO}_2$ (IoP)
Gas composition	150 sccm $\text{SiH}_4$ , 700 sccm $\text{N}_2\text{O}$	10 sccm Ar, 2 sccm $\text{O}_2$
Power	MW, 20 W	RF, 200 W
Process pressure	1.3 mbar	1 Pa
Substrate temperature	300 °	RT
Growth rate	67.5 nm/min	8 nm/min

Zinc oxide layers were deposited in cooperation with Ing. Petr Novák Ph.D. from University of West Bohemia in Pilsen. The deposition was performed in a BOC Edwards TF 600 coating system equipped with two magnetrons connected to a radio-frequency (RF) and direct-current (DC) power supplies.

Table 3.2: Conditions used for deposition of zinc oxide layers using magnetron sputtering

RF power (W)	Discharge voltage (V)	Gas composition		Pressure (Pa)	Temperature (°C)
		$\text{O}_2$ (sccm)	Ar (sccm)		
600	860-1060	4	3	1	350

#### **SAW device fabrication at CEITEC**

For metal deposition, the substrate was loaded in ion-beam sputtering instrument equipped with two Kaufman ion-beam sources (IBS). The pre-cleaning procedure was done for 5 minutes with Ar ions at low energy of 36 eV. Then was used primary IBS for deposition of 3 nm thick Ti adhesion layer using Ar ions with energy of 600 eV. This step was followed by deposition of 200 nm thick Al layer employing Ar ions with energy of 900 eV.

Shaping of interdigitated electrodes was done using UV lithography employing positive photoresist and etching using  $\text{BCl}_3/\text{Cl}_2$  plasma mixture in RIE instrument. The photoresist was then removed using dimethylsulfoxid (DMSO) for 10 minutes at 80 °C, rinsed by demineralized water and dried by compressed nitrogen.

Such cleaned wafer was then placed to the PECVD instrument for deposition of 2.5  $\mu\text{m}$  thick  $\text{SiO}_2$  layer. Consequent etching of  $\text{SiO}_2$  was done using mixture of  $\text{CHF}_3/\text{Ar}$  plasma using RIE method. When the etching of  $\text{SiO}_2$  was done, wafer was cleaned using the same procedure as is described before. Wafer was then covered using positive photoresist and cut into single chips using dicing saw.

#### **SAW device characterization**

Fabricated LW-SAW sensors were characterized using a vector network analyzer Agilent E8364B and Summit 9000 Analytical Probe Station with Infinity probes at Institute of Physics, CAS. Reflection  $S_{11}$  and  $S_{22}$  and transmission  $S_{21}$  and  $S_{12}$  scattering parameters were measured in magnitude and phase at the room temperature.

### **3.3 Diamond layers deposition & characterization**

#### **CVD diamond depositions**

Thin nanocrystalline diamond (NCD) layers were deposited using MW-LA-PECVD apparatus at a low temperature ( $< 500$  °C) and AX5010

### 3.3 Diamond layers deposition & characterization

---

apparatus (Seki Diamond System) for conventional NCD deposition. The BDD layers were grown on the conductive (100)-oriented 10x10 mm silicon (cSi) substrates (ON Semiconductor, Czech Republic). Prior the diamond seeding, samples were cleaned using sonication in acetone, isopropylalcohol and hot distilled water for 5 minutes in each followed by 10 minutes in  $\text{H}_2\text{SO}_4 + \text{H}_2\text{O}_2$  mixture (1:1) and sonicated twice in hot water for 5 minutes. As thin  $\text{SiO}_2$  layer form naturally on Si surface, all samples were etched for 30 seconds in hydrofluoric acid (HF) and rinsed twice in hot water in ultrasonic bath for 5 minutes.

Prior to NCD growth, LW-SAW devices and cSi substrates were seeded with nanodiamond particle water based colloids (NanoAmando®B from NanoCarbon Research Institute Ltd., average mean crystal size of 4-6 nm) by spin coating (30 s at 3000 rpm). The IDTs contact pads of LW-SAW sensors were mechanically protected by clean lab tape as solid mask (F04xx tape from Semiconductor Equipment Corp.) to ensure they would not be coated with insulating diamond. Conditions for NCD layers deposition are reported in tables 3.3 and 3.4.

Table 3.3: Intrinsic and boron doped diamond layers deposition conditions at low temperature

	Intrinsic NCD	BDD
Gas composition	92 % $\text{H}_2$ , 5 % $\text{CH}_4$ , 3 % $\text{CO}_2$	8 % $\text{CH}_4$ , 40 % $\text{H}_2$ , 150 % $\text{B}_2\text{H}_6$ , 1.75 % $\text{CO}_2$ (sccm)
MW power	2 · 2.75 kW	2 · 2.7 kW
Process pressure	0.25 mbar	0.25 mbar
Substrate temperature	320 - 500 °C	450 - 600 °C

Table 3.4: BDD layers deposition conditions in AX5010 apparatus

<b>Process gas flow (sccm)</b>	2.5 $\text{CH}_4$ , 492 $\text{H}_2$ , 5 $\text{B}_2\text{H}_6$
<b>MW power (kW)</b>	1.15
<b>Process pressure (mBar)</b>	50
<b>Substrate temperature (°C)</b>	1000

#### Morphology characterization

The morphology and the roughness of the NCD layers were investigated by Atomic force microscopy (AFM) using a Dimension Icon ambient AFM in Peak Force Tapping mode with Tap150Al-g tips and Tescan FERA3 scanning electron microscope (SEM).

#### Raman spectroscopy

The quality of diamond layer was investigated using Raman spectroscopy using Renishaw InVia Raman microscope with a 488 nm excitation laser at a power of 25 mW at 20 °C. Raman spectra were normalized to the diamond peak.

#### Electrochemical characterization of BDD layers

To investigate the electrochemical performance of fabricated BDD layers, cyclic voltammetry (CV) was recorded in a supporting electrolyte 1 mol·L<sup>-1</sup> KCl and two different redox probes, namely: [Ru(NH<sub>3</sub>)<sub>6</sub>]<sup>3+/2+</sup> (surface insensitive probe) and [Fe(CN)<sub>6</sub>]<sup>3-/4-</sup> (surface sensitive probe) and electrochemical impedance spectroscopy (EIS). Cyclic voltammograms were recorded with a scan rate of  $v = 100 \text{ mV}\cdot\text{s}^{-1}$  (5x) in the 1 mmol·L<sup>-1</sup> [Ru(NH<sub>3</sub>)<sub>6</sub>]<sup>3+/2+</sup> in 1 mol·L<sup>-1</sup> KCl and 1 mmol·L<sup>-1</sup> [Fe(CN)<sub>6</sub>]<sup>3-/4-</sup> in 1 mol·L<sup>-1</sup> KCl solutions.

EIS spectra were recorded in the frequency range  $f = 100 \text{ kHz} - 0.1 \text{ Hz}$  in the 1 mmol·L<sup>-1</sup> [Fe(CN)<sub>6</sub>]<sup>3-/4-</sup> in 1 mol·L<sup>-1</sup> KCl solution. All experiments were carried out at room temperature.

## 4 | Results

This chapter summarizes the work carried out within this Thesis. The development of biosensors is complex task involving optimalization and fabrication of physical transducer, production of biosensing elements and their immobilization on the surface of the transducer. All these important steps of biosensor development are discussed within the following eight chapters. Three of them are theoretical about FEM simulations of LW-SAW sensors, two chapters describes experimental work on LW-SAW sensors, one chapter is devoted to the production and purification of his-tagged bacteriophage tail fibers, one chapter focuses on functionalization of boron doped diamond layers in order to attach produced tail fibers to the BDD surface and last chapter summarizes work on the QCM sensors with BDD layer and its functionalization.

### 4.1 FEM simulations of the properties of diamond coated LW-SAW sensors

The aim of this chapter was to investigate the behavior of the LW-SAW sensors after the addition of the diamond layer on top of the sensitive area of the sensor's surface. This is important for proper choice of the materials and to distinguish the parameters of the diamond coated LW-SAW sensors, such as guiding layer thickness, IDTs spatial period and diamond layer thickness, to obtain sensor with the best performance and sensitivity. The results were used to design sensors fabricated in the following chapters.

Three most commonly used piezoelectric substrates for LW devices were investigated - quartz, lithium tantalate ( $\text{LiTaO}_3$ ) and lithium niobate ( $\text{LiNbO}_3$ ) in combination with two mostly used guiding layers materials -  $\text{SiO}_2$  and  $\text{ZnO}$ .

Theoretical simulations were carried out using COMSOL Multiphysics software with model described in the section Methods, Basic

model. The dispersion curves were calculated for guiding layer normalized thickness  $h_{\text{guid}}/\lambda$  between 0.01 and 1 by fixing  $\lambda = 10 \mu\text{m}$  and varying the thickness of  $\text{SiO}_2$  or  $\text{ZnO}$  layer for different thicknesses of the diamond coating  $h_{\text{NCD}}$ .

Figure 4.1 shows an example of a dispersion curves obtained for ST-cut quartz substrate with  $\text{SiO}_2$  guiding layer. Figure 4.1a) shows that the phase velocity is constant for  $h_{\text{SiO}_2}/\lambda$  below 0.04 for uncoated LW-SAW sensor with  $\text{SiO}_2$  guiding layer and decreases above this value. This is attributed to trapping of the acoustic waves in the  $\text{SiO}_2$  guiding layer with slower shear velocity ( $2850 \text{ m}\cdot\text{s}^{-1}$ ) than the piezoelectric substrate. The phase velocity increase with the thickness of the NCD layer. Figure 4.1c) shows the optimal sensitivity is obtained for silicon oxide normalized thickness  $h_{\text{SiO}_2}/\lambda$  between 0.1 and 0.5 and it is shifting the highest sensitivity to higher  $h_{\text{SiO}_2}/\lambda$  values with higher diamond coating thicknesses. Within this range of normalized thickness  $h_{\text{SiO}_2}/\lambda$ ,  $K^2$  is decreasing from 0.25 to 0.1 %, (see figure 4.1b)). The last graph 4.1d) shows the sensitivity as a function of diamond normalized thickness  $h_{\text{NCD}}/\lambda$  for  $h_{\text{SiO}_2}/\lambda$  equals to 0.15 and 0.3. Steep decrease in sensitivity is observed for increasing  $h_{\text{NCD}}/\lambda$  reaching zero sensitivity at  $h_{\text{NCD}}/\lambda = 0.007$  and  $0.03$  for  $h_{\text{SiO}_2}/\lambda = 0.15$  and  $0.3$  respectively, which confirms the graph 4.1c) and highlights the importance of thin diamond coating.

Simulations of the other piezoelectric materials combined with silicon oxide or zinc oxide guiding layer revealed comparable behavior of diamond-coated LW-SAW sensors, that can be summarized in following points:

- Phase velocity increases after adding a thin diamond coating on top of LW-SAW device. This is attributed to the increasing stiffness of the sensor's surface.
- The highest sensitivity of LW-SAW sensor is obtained in the region of the largest dispersion of the phase velocity and sensitivity steeply decreases with increasing diamond coating thickness.

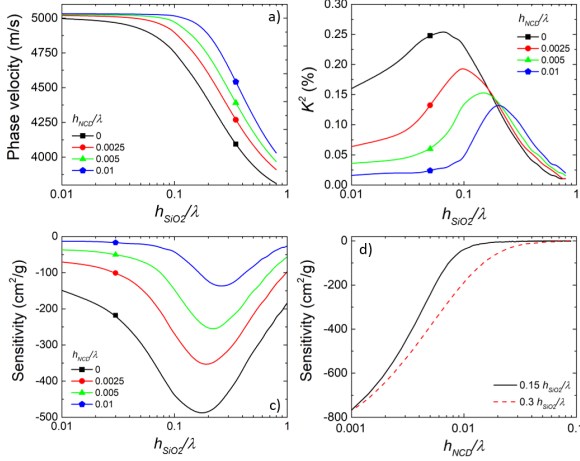


Figure 4.1: Dispersion curves for a) phase velocity and b)  $K^2$  and c) sensitivity as a function of silicon normalized thickness  $h_{SiO_2}/\lambda$  for different thicknesses of diamond coating for Diamond/SiO<sub>2</sub>/ST-cut quartz structure and d) sensitivity as a function of thickness of diamond coating normalized thickness for two different silicon normalized thickness  $h_{SiO_2}/\lambda$

- The drop in sensitivity after adding of diamond coating is much higher for LiTaO<sub>3</sub> and LiNbO<sub>3</sub> substrate in comparison with ST-cut quartz substrate. This is attributed to the fact, that LiTaO<sub>3</sub> and LiNbO<sub>3</sub> substrates do not generate pure shear horizontal waves, but leaky waves and the acoustic energy is dissipated into the substrate.
- Electromechanical coupling coefficient decreases after adding of a thin diamond layer.
- In comparison with SiO<sub>2</sub> guiding layer, ZnO guiding layer provides higher electromechanical coupling coefficient due to its own piezoelectric properties.

In the design of LW-SAW sensor, it is necessary to take into account

several limitations inerrant to the sensor fabrication processes. The resolution of the optical lithography method to pattern IDTs electrodes is approximately  $2\ \mu\text{m}$  (using the apparatus MicroWriter at IoP), which limits the IDTs spatial period to  $10\ \mu\text{m}$ . Deposition of  $\text{SiO}_2$  guiding layer thicker than  $3\ \mu\text{m}$  is difficult due to high mechanical stress in the layer and the possible delamination. Deposition of very thin NCD layer is also limited, due to the necessary minimum thickness to obtain a coalesced and pin-hole free diamond layer.

$36^\circ\text{YX}$   $\text{LiNbO}_3$  substrate has very high coupling factor, but the substrate breaks extremely easily when exposed to abrupt thermal shock, which makes it difficult to handle during fabrication process including high temperature diamond deposition. The  $36^\circ\text{YX}$   $\text{LiTaO}_3$  substrate possesses low insertion loss and large  $K^2$ , which provide advantages over the other substrates, such as quartz cuts. The main shortcomings of  $\text{LiTaO}_3$  substrate are 1) its poor thermal stability caused by high  $TCF$  and 2) it excites leaky waves, which leads to the increase of damping in liquid environment [12]. Quartz is the only common substrate material that offers cuts generating purely shear horizontal polarized waves, but they possess weak coupling coefficient. [13] From the fabrication point of view, Curie temperature needs to be taken into account, which is lowest for quartz ( $573\ ^\circ\text{C}$ ) [14],  $665\ ^\circ\text{C}$  for  $\text{LiTaO}_3$  [15] and  $1140\ ^\circ\text{C}$  for  $\text{LiNbO}_3$  [16].

From the reasons stated above, we decided to fabricate LW-SAW sensors using ST-cut quartz substrate and  $\text{SiO}_2$  guiding layers. The decrease of sensitivity with the addition of the continuous diamond layer on top of LW-SAW sensors using different piezoelectric substrates lead us to think about another types of diamond coating, such as discrete diamond coating or phononic metamaterials to increase the electromechanical coupling coefficient and the sensitivity of the LW-SAW devices. These ideas will be discussed in following chapters.

## 4.2 LW-SAW devices with continuous and discrete NCD coatings

This study aims to investigate the difference between continuous and discrete NCD layer coating on LW-SAW sensors properties and is based on the following publication [17].

- **L. Drbohlavová**, L. Fekete, V. Bovtun, M. Kempa, A. Taylor, Y. Liu, O. Bou Matar, A. Talbi, and V. Mortet. Love-wave devices with continuous and discrete nanocrystalline diamond coating for biosensing applications. *Sensors and Actuators, A: Physical*, **298**, 2019

### Methods

Diamond/SiO<sub>2</sub>/ST-cut quartz structures have been simulated using COMSOL Multiphysics software using the basic model described in the Methods. The theoretical study of the coalescence effect of diamond on the propagation of SH waves was carried out in three steps: 1/ deposition of an increasing number (4, 9, 16, 36, 64, 144) of diamond grains (modeled as cubes) with a fixed width (274 nm) and increasing thickness over the range of 45 nm to 200 nm (see Figure 4.2 a-b), 2/ followed by the connection of diamond grains resulting in a decreasing number (64, 36, 16, 9, 4, 1) of grains but keeping the whole surface covered (see Figure 4.2 c-d). The thickness of the diamond cubes increased over the range of 210 to 420 nm. And finally, 3/ the growth of a fully coalesced diamond layer. The results of this study were compared to the growth of a diamond layer and the effect of a rapid coalescence.

LW-SAW sensors were fabricated at IoP on ST-cut quartz substrates with a 1.6  $\mu\text{m}$  thick amorphous SiO<sub>2</sub> layer and aluminum IDTs with a spatial period of 16  $\mu\text{m}$  resulting in a normalized SiO<sub>2</sub> thickness of 0.1. Consecutive depositions of NCD layers were carried out at low temperature by MW-LA-PECVD apparatus in order to determine the effect of diamond grain size, coalescence and diamond thickness.

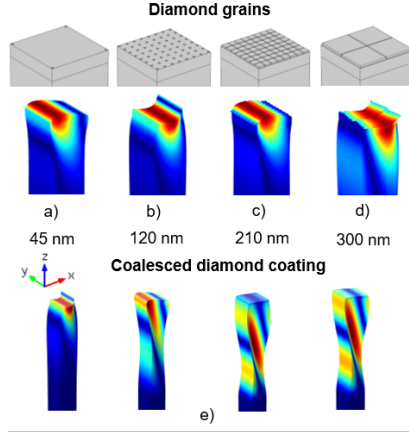


Figure 4.2: Love wave mode shapes for  $\text{SiO}_2/\text{ST-cut}$  quartz structures with different numbers of NCD grains: a) 4 grains,  $h_{\text{NCD}}=45$  nm, b) 64 grains,  $h_{\text{NCD}}=120$  nm, c) 64 grains covering whole surface,  $h_{\text{NCD}}=210$  nm, d) 4 grains,  $h_{\text{NCD}}=300$  nm and e) coalesced NCD layer with the same thicknesses.

Figure 4.3 shows AFM pictures of deposited NCD layers with different nucleation density.

## Results

Figure 4.4 shows the effect of NCD thickness on the experimentally recorded normalized phase velocity that is compared with simulated results. Phase velocity was normalized to 4373 m/s (minimum measured velocity) and 5060 m/s (propagation velocity value for acoustic waves in ST-cut quartz substrates). For coalesced NCD layers the phase velocity steeply increases for initial values of NCD thickness and becomes almost constant as it approaches 5000 m/s. This result indicates that the Love waves are no longer trapped within the  $\text{SiO}_2$  guiding layer, but that they propagate only within the quartz substrate (see figure 4.2e). However, after deposition of discrete NCD grains, the phase velocity increases slightly for the first two depositions, this is attributed to annealing of the quartz substrate and amorphous  $\text{SiO}_2$  layer during

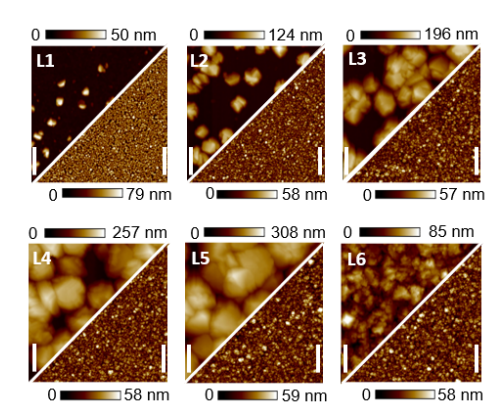


Figure 4.3: AFM images of deposited NCD layers with different nucleation density: 1) deposition of NCD grains (upper part, white bar indicates 270 nm) and 2) deposition of closed NCD layers (lower part, white bar indicates 1  $\mu\text{m}$ )

diamond deposition, then the phase velocity starts to decrease until the NCD layer coalesces. The additional mass on the surface of the sensor created by isolated grains slows down the acoustic waves, which results in a decrease in operating frequency. It can also be observed, that the phase velocity is lower than for coalesced NCD coatings, which indicates improved confinement of Love waves in the guiding layer, which can be clearly observed in the figure 4.2 and therefore ensure a higher sensitivity for the discrete NCD grain coated LW-SAW sensors than for the sensors with coalesced NCD layers.

To explain results in depth, we calculated the band structure of SH modes (SH ratio  $> 0.5$ ) for each of the cases shown in Figure 4.2c. The result is shown in Figure 4.5, X points are the irreducible Brillouin zone limit of the unit cell in the  $x$  direction (cell parameter is fixed to 10  $\mu\text{m}$ ). The black continuous and broken lines correspond to the shear bulk mode in quartz and  $\text{SiO}_2$  substrates respectively. In the case of coalesced NCD layers, the Love mode is located above the limit of the substrate shear mode. This means that the mode radiates into the bulk of the substrate, which is confirmed by displacement field distribution

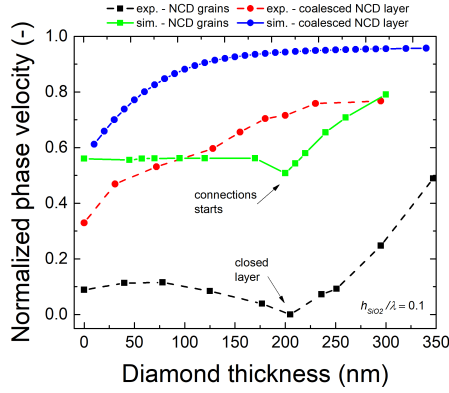


Figure 4.4: Normalized phase velocity of a Love waves as a function of NCD layer thickness from simulation (solid lines) and from experimental measurements (dashed lines) for coalesced NCD layers (circles) and discrete NCD grains (squares) on  $\text{SiO}_2/\text{ST-cut}$  quartz structure.

(see Figure 4.2e). For discrete NCD grain coating, the Love mode is below the limit of the substrate shear mode, whilst approaching the limit of the Brillouin zone which implies a good confinement of the mode in the  $\text{SiO}_2$  layer.

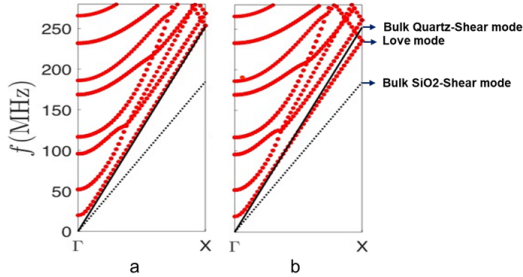


Figure 4.5: Band structure of unit cell: geometrical parameters case (Figure 5c) and cell parameter fixed to  $10 \mu\text{m}$ . a) coalesced NCD layer and b) discrete NCD grains

## Conclusions

- Increasing phase velocity with diamond coating due to the increasing rigidity of the sensor's surface for continuous diamond layers.
- Decreasing phase velocity for isolated diamond grains due to mass loading effect.
- Increase of phase velocity above 5060 m/s was not observed, confirming that Love waves are not propagating within the deposited diamond layer.

## 4.3 Enhancing the sensitivity of SAW sensors using the diamond surface phononic metamaterials

Part of this work has been presented on the international conference 2020 Virtual MRS Spring/Fall Meeting & Exhibit, November 27<sup>th</sup> – December 4<sup>th</sup> as the poster presentation and was nominated for the "Best poster Award".

### Diamond PnMs on SiO<sub>2</sub> guiding layer

At first, the band structure was calculated to investigate different acoustic modes for the diamond PnMS ( $r_p = 250$  nm,  $h_p = 750$  nm) on SiO<sub>2</sub> guiding layer ( $h_{SiO_2} = 1.5$   $\mu$ m) with lattice period  $a = 1$   $\mu$ m, and is shown in the figure 4.6).

Gray area is the radiation zone, where the waves start to propagate in the substrate bulk. Upper black dotted line is dispersion curve of the fast shear waves in the quartz substrate, lower black dotted line denotes the dispersion curve for shear waves in silica layer, calculated according to  $v = \frac{2\pi f}{k}$ . Modes located between these two lines are guided in silica layer. Color of modes is based on the SH ratio, blue color denotes Rayleigh waves and green color refers to the Love waves. When the frequency of the Love wave match with the resonance frequency of the

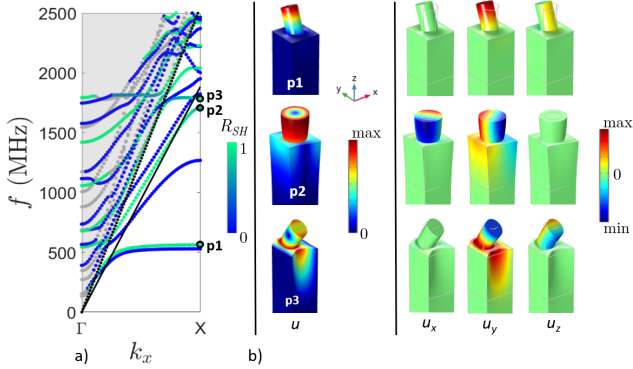


Figure 4.6: a) Band structure of PnMs based on pillar along  $\Gamma$ -X direction for 90ST-quartz +  $\text{SiO}_2$  layer + diamond pillar (blue denotes Rayleigh wave, green color means Love waves, gray lines are bulk waves) and b) mode shapes of SH surface modes with shown  $u_x, u_y$  and  $u_z$  deformation components

pillar, we obtain wave coupling resulting in local resonance. These coupled modes are going below the dispersion curve for silica layer (lower black dotted lines), which means localization of the acoustic energy in the pillar. This is confirmed by  $u_y$  displacement component of SH waves at the X point of the BZ, shown in the figure 4.6b)). p1 mode ( $f = 562.3$  MHz) is localized flexion pillar mode and p3 ( $f = 1789$  MHz) is Love mode guided in the  $\text{SiO}_2$  layer coupled with the pillar. p2 ( $f = 1706$  MHz) is indicated by petrol color in the band structure as it is the torsional mode having also  $u_x$  displacement component. Based on these results, the calculation of the sensitivity was carried out for the slowest flexion pillar mode (p1), as the acoustic energy is confined well in the pillar.

As can be seen from the graph 4.7, the sensitivity is steeply decreasing for very small values of  $r/a$ , for  $r_p = 0.25$ ,  $r/a < 0.075$ , which is equal to  $a = 3.3 \mu\text{m}$ , for  $r_p = 0.35$ ,  $r/a < 0.125$ , resulting in  $a = 2.5 \mu\text{m}$ . From these  $r/a$  values and higher, the sensitivity remains constant, which means, that we don't need to decrease lattice parameter

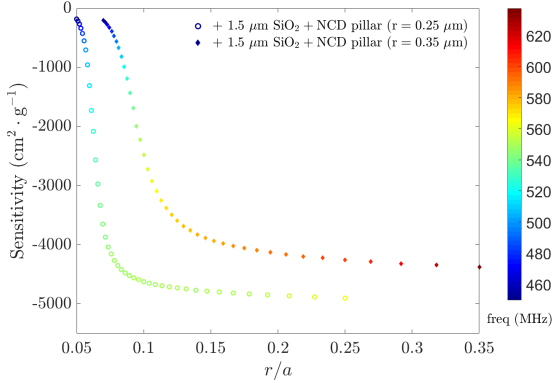


Figure 4.7: Sensitivity as a function of filling factor  $r/a$  for diamond PnMs on 1.5  $\mu\text{m}$  thick  $\text{SiO}_2$  guiding layer, pillar radii  $r = 0.25$  and  $0.35 \mu\text{m}$ ,  $h_p = 750 \text{ nm}$ .

$a$  as much as possible to obtain better sensitivity. This result is interesting from the fabrication point of view, as fabrication of high density pillars is more complex.

### $\text{SiO}_2$ PnMs on $\text{SiO}_2$ guiding layer

For comparison with diamond pillars, the same work was done using  $\text{SiO}_2$  pillar with the same geometry parameters ( $r_p = 250 \text{ nm}$ ,  $h_p = 750 \text{ nm}$ ,  $h_{\text{SiO}_2} = 1.5 \mu\text{m}$  and  $a = 1 \mu\text{m}$ ). At first, the band structure was calculated to see the acoustic modes and it can be seen on the figure 4.8a).

As for the diamond pillar, p1 mode ( $f = 456 \text{ MHz}$ ) is localized flexion pillar mode and p3 ( $f = 1618.6 \text{ MHz}$ ) is Love mode guided in the  $\text{SiO}_2$  layer coupled with the pillar, p2 ( $f = 1100.5 \text{ MHz}$ ) torsional mode also with  $u_x$  displacement component. p4 mode is already above the dispersion curve for shear waves in silica layer (black line) and as can be seen from mode shapes, the acoustic energy is located in the guiding layer.

The sensitivity study calculated for the p1 mode revealed the same

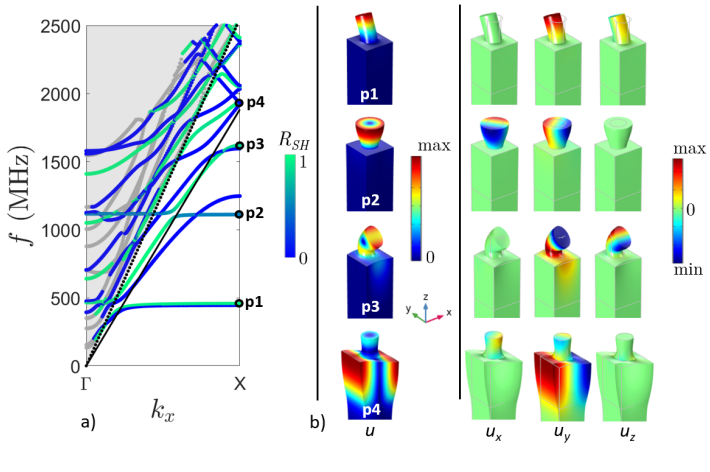


Figure 4.8: a) Band structure of PnMs based on pillar along  $\Gamma$ -X direction for 90ST-quartz +  $\text{SiO}_2$  layer +  $\text{SiO}_2$  pillar (blue denotes Rayleigh wave, green color means Love waves, gray lines are bulk waves) and b) mode shapes of SH surface deformation modes with shown  $u_x, u_y$  and  $u_z$  deformation components

trends as for diamond PnMs, but the  $\text{SiO}_2$  pillars are more sensitive than the diamond ones. This is done by mechanical properties of the used materials. However, thanks to the properties of diamond (chemical inertness, biocompatibility, possibility of surface functionalization), it is more convenient material for bioapplications.

## Conclusions

This work builds on the results from the chapter 4.2, where we confirmed radiation of the Love mode into the bulk of the substrate for continuous diamond coatings and good confinement of the Love mode in the  $\text{SiO}_2$  guiding layer, when the discrete diamond grains were used. The aim of this chapter was to study confinement of the acoustic waves in the PnMs and improvement of the sensitivity of such SAW sensors. In the band structure we observed coupled modes going below the dispersion curve for silica layer, that confirmed localization of the acoustic

energy in the pillar for both studied materials (diamond and  $\text{SiO}_2$ ) of pillars. Sensitivity was studied as a function of a filling factor  $r/a$  giving the result, that the lattice parameter  $a$  does not need to be decrease as much as possible to obtain better sensitivity of LW-SAW sensors with PnMs. Also the highest sensitivity obtained from these simulations for diamond PnMs is around  $5000 \text{ cm}^2 \cdot \text{g}^{-1}$ , which is much higher than the sensitivity obtained from the simulations for continuous diamond coating. This theoretical study is promising for the fabrication of highly sensitive LW-SAW sensors with diamond PnMs for biosensing applications.

#### 4.4 Experimental investigation of the properties of diamond coated LW-SAW sensors

To verify theoretical results obtained from COMSOL simulations, LW-SAW devices with different IDTs spatial periods were fabricated and characterized.

##### 4.4.1 ST-cut quartz LW-SAW sensors with $\text{SiO}_2$ guiding layer

Fabrication was carried out using 90 degrees rotated ST-cut quartz substrate to support excitation of SH waves, 200 nm thick aluminum electrodes and 2.5  $\mu\text{m}$  thick amorphous  $\text{SiO}_2$  guiding layer. Sensors with different IDTs spatial periods were prepared to obtain several silicon oxide normalized thicknesses  $h_{\text{SiO}_2}/\lambda$ . To study the effect of diamond coating on LW-SAW sensors, NCD layers with thicknesses of 57 nm, 100 nm and 133 nm were deposited on the  $\text{SiO}_2$  guiding layers.

Figure 4.9a) shows example of the transmission coefficient  $S_{21}$  for sensor with spatial period  $\lambda = 16 \mu\text{m}$ . Increase of resonant frequency after deposition of 100 nm thick NCD layer can be clearly observed. Figure 4.9b) gives together the phase velocity dispersion curves obtained by simulations with the experimental data. It can be seen, that the experimental and modeled phase velocity trends are very similar.

But the phase velocity from the experiment is lower than the calculated one, mainly for the diamond-coated LW-SAW sensor. This shift is attributed to different mechanical properties used in simulations than is in the real sensors.

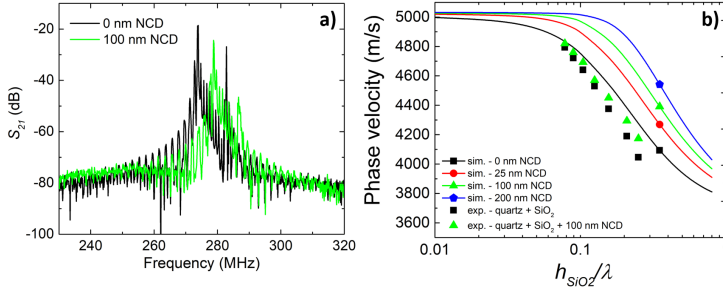


Figure 4.9: a) Spectra of transmission coefficient  $S_{21}$  for LW-SAW sensor without and with NCD layer,  $\lambda = 16 \mu\text{m}$ ,  $h_{SiO_2} = 2.5 \mu\text{m}$  and b) phase velocity dispersion curves obtained experimentally and from simulations

After this experiment, simulations were repeated with changing Young's modulus  $E$  of SiO<sub>2</sub> guiding layer and diamond layer to obtain a better agreement with the experimental data. Figure 4.10 shows the phase velocity dispersion curves obtained from simulation with corrected Young's modulus in comparison with experimental data. Very good agreement of data can be seen for  $E_{SiO_2} = 60 \text{ GPa}$  and  $E_{NCD} = 240 \text{ GPa}$ . The value of  $E_{NCD}$  is much lower than previously used value of 1050 GPa of the single crystal diamond.

To support this result, the nanoindentation measurements were done on the nanocrystalline diamond layers. Obtained values of hardness and reduced modulus are shown in the figure 4.11. As the NCD layer are very thin and the indentation depth was around 20  $\mu\text{m}$ , the influence of the substrate cannot be avoided. The reduced elastic modulus for NCD layers is lower than obtained from corrected simulations, which may reflect the influence of the substrate. Nanoindentation measurement done on the 310 nm thick NCD layers on silicon substrates

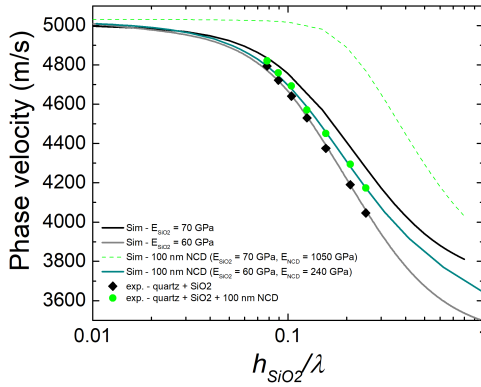


Figure 4.10: Phase velocity dispersion curves obtained experimentally and from simulations with corrected Young's modulus of SiO<sub>2</sub> guiding layer and thin NCD layer

gave value of reduced elastic modulus equal to  $249 \pm 20$  GPa [18], which is close to the value obtained from simulation.

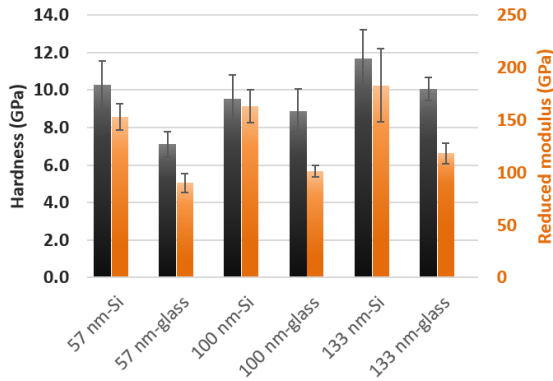


Figure 4.11: Hardness and reduced elastic modulus of thin NCD layers with different thicknesses on two types of substrates

### Sensitivity study

According to simulation results, sensitivity of LW-SAW sensors should decrease after the NCD coating for all types of substrates and guiding layers.

First pilot study was carried out using LW-SAW sensors fabricated at IoP. They consisted of 90ST-cut quartz substrate, 200 nm thick aluminum electrodes with two different spatial periods  $\lambda = 16$  and 32  $\mu\text{m}$  and 1.6  $\mu\text{m}$  thick  $\text{SiO}_2$  guiding layer and were coated by 100 nm thin NCD layers.

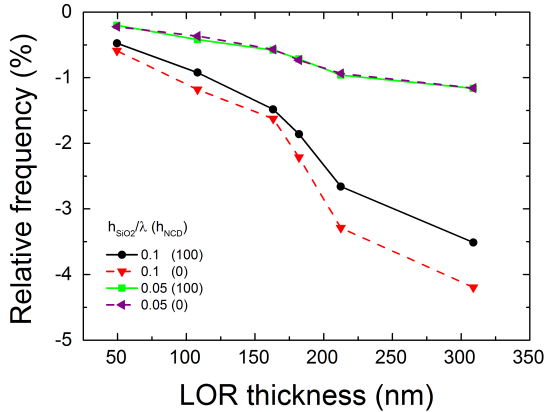


Figure 4.12: Relative center frequency shift as a function of the LOR thickness for ST-cut quartz/ $\text{SiO}_2$  sensors with 100 nm NCD thickness for two different silicon normalized thicknesses  $h_{\text{SiO}_2} = 0.1$  and 0.05

Figure 4.12 clearly shows a decrease in center resonant frequency with increasing LOR thickness caused by mass loading. The frequency shifts of the uncoated and NCD coated sensor are comparable for normalized thicknesses  $h_{\text{SiO}_2}/\lambda = 0.05$ , which means that the sensitivity is not changed by deposition of a 100 nm thin NCD layer. But we can observe slight decrease in sensitivity for diamond coated sensors with  $h_{\text{SiO}_2}/\lambda = 0.1$  in comparison with uncoated one. These results are not

in agreement with theoretical calculations, as the high decrease in sensitivity after NCD coating has been expected. Expected results is, that the LW-SAW sensors with  $h_{SiO_2}/\lambda = 0.1$  exhibit higher sensitivity of  $1170 \text{ cm}^2/\text{g}$  compared to  $340 \text{ cm}^2/\text{g}$  of the sensor with  $h_{SiO_2}/\lambda = 0.05$ .

To study the effect of the thickness of NCD layer on the sensor's sensitivity, the LW-SAW sensors with different NCD thicknesses were coated by 74 nm thick photoresist layer and the frequency shift was measured. To compare experimental results with theoretical simulations, new simulations were performed. The thickness of silicon oxide guiding layer was fixed to  $2.5 \text{ }\mu\text{m}$  with Young's modulus  $E_{SiO_2} = 60$  and  $70 \text{ GPa}$  and the acoustic wavelength was changing in the range of  $2 - 240 \text{ }\mu\text{m}$ , which gives the  $h_{NCD}/\lambda = 0.0104 - 1.25$ . Thickness of NCD layer was fixed to 100 and 133 nm with Young's modulus  $E_{NCD} = 240 \text{ GPa}$ . To calculate the sensitivity, 74 nm thick PMMA layer ( $\rho = 1.02 \text{ g}\cdot\text{cm}^{-3}$ ) was added on the model's surface.

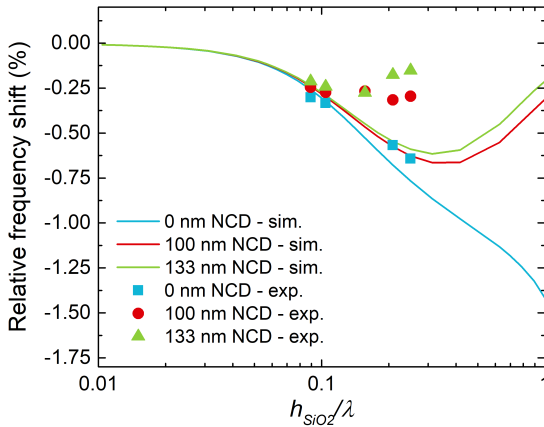


Figure 4.13: Comparison of relative center frequency shift obtained experimentally and from simulation as a function of the silicon normalized thickness for ST-cut quartz/SiO<sub>2</sub> sensors with different NCD thicknesses

Graph 4.13 shows simulated relative frequency shift curves compared to the values obtained from the experiment. The diamond normalized thickness is changing for each wavelength. Hence for larger  $\lambda$ , there is not an impact of adding thin diamond layer on the sensitivity, as the  $h_{NCD}/\lambda$  is very small, e.g. for  $\lambda = 240 \text{ }\mu\text{m}$ ,  $h_{NCD}/\lambda = 0.000417$ . The influence of diamond layer on the sensitivity can be seen for the values of  $h_{SiO_2}/\lambda = 0.16$  and higher, where the  $\lambda = 15 \text{ }\mu\text{m}$  and  $h_{NCD}/\lambda = 0.0067$ . As the  $h_{NCD}/\lambda$  becomes higher, the impact of diamond layer is getting more significant and reduces the sensitivity.

#### 4.4.2 36°YX LiTaO<sub>3</sub> LW-SAW sensors with SiO<sub>2</sub> guiding layer

The same study was carried out also using the LW-SAW sensors fabricated on black 36°YX LiTaO<sub>3</sub> substrates with 200 nm thick aluminum electrodes and 2.5  $\mu\text{m}$  thick amorphous SiO<sub>2</sub> guiding layer and NCD layers were deposited in three different thicknesses - 55, 65 and 98 nm.

Example of the transmission coefficient  $S_{21}$  for sensor with spatial period  $\lambda = 16 \text{ }\mu\text{m}$  is shown in the figure 4.14a), where small resonant frequency shift after NCD layer deposition can be seen. Figure 4.14b) shows comparison of phase velocity dispersion as a function of  $h_{SiO_2}/\lambda$  obtained experimentally and from simulations. Experimentally obtained phase velocity is lower than the one from simulations. Also, the experimental data are scattered and does not follow one line clearly. This phase velocity drop in experimental data compared to simulation ones are possibly caused by different mechanical properties in real sensors than in simulations as was discussed for ST-cut quartz/SiO<sub>2</sub> sensors in previous section.

Nanoindentation measurement was carried out on the diamond layers deposited on this set of samples and also on the SiO<sub>2</sub> layer deposited on LiTaO<sub>3</sub> samples. The values for NCD layer with thicknesses 55 and 65 nm are comparable to the values obtained from nanoindentation measurement discussed in previous section. On the contrary, measured reduced modulus 82 GPa for SiO<sub>2</sub> layer is higher than the theoretical

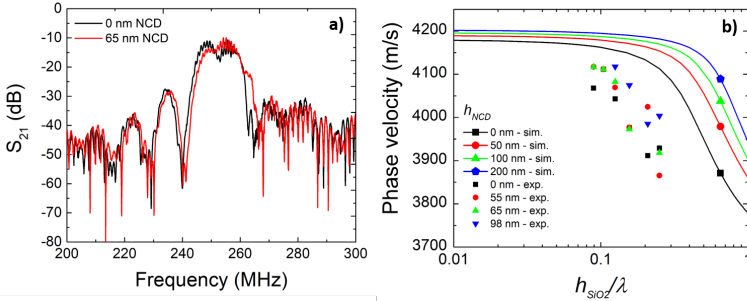


Figure 4.14: a) Spectra of transmission coefficient  $S_{21}$  for LW-SAW sensor without and with NCD layer,  $\lambda = 16 \mu\text{m}$ ,  $h_{SiO_2} = 2.5 \mu\text{m}$  and b) phase velocity dispersion curves obtained experimentally and from simulations

value 70 GPa.

### 4.4.3 LW-SAW sensors with ZnO guiding layer

Deposition of diamond layer on the ZnO layer is problematic, as ZnO layer can be etched during the deposition. Therefore test samples were prepared at first. Three types of samples were prepared: 1) Si substrate, 380 nm thick ZnO layer, 2) Si substrate, 380 nm thick ZnO layer and 90 nm thin  $\text{Al}_2\text{O}_3$  layer and 3) Si substrate, 380 nm thick ZnO layer and 50 nm thin  $\text{SiO}_2$  layer. 150 nm thin NCD layers were deposited using standard conditions. The best result was obtained for Si/ZnO/ $\text{SiO}_2$  samples, where we can observe closed NCD layer and  $\text{SiO}_2$  layer protected ZnO layer against etching during the NCD growth.

#### Diamond coated-SAW with ZnO guiding layer

1.9  $\mu\text{m}$  thick ZnO guiding layer was deposited on the 90ST-cut quartz and  $36^\circ\text{YX}$   $\text{LiTaO}_3$  sensors with aluminum electrodes with spatial periods  $\lambda = 32, 24$  and  $16 \mu\text{m}$ . Resonant peak can be clearly seen for sensors without guiding layer and with ZnO layer. An increase in insertion loss is observed after the deposition of the thin  $\text{SiO}_2$  layer. To our surprise

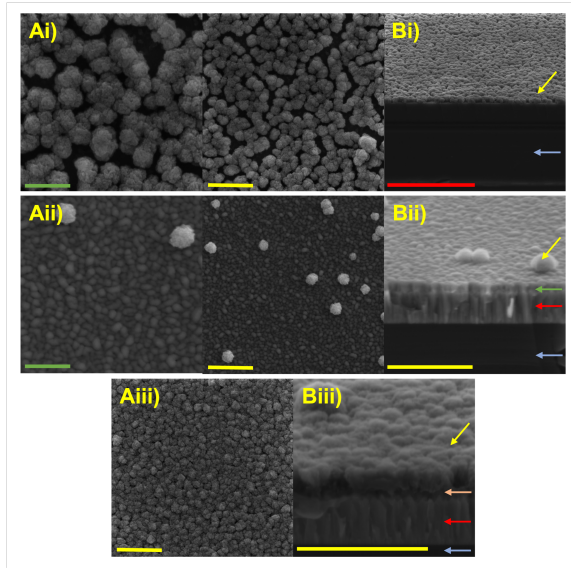


Figure 4.15: A) SEM micrographs of NCD layers deposited on ZnO layer and B) cross-section view, i) Si/ZnO, ii) Si/ZnO/Al<sub>2</sub>O<sub>3</sub> and iii) Si/ZnO/SiO<sub>2</sub>, green bar indicates 500 nm, yellow bar 1  $\mu\text{m}$  and red bar is 5  $\mu\text{m}$ , yellow arrow shows NCD layer, red arrow ZnO layer, green arrow Al<sub>2</sub>O<sub>3</sub>, orange arrow SiO<sub>2</sub> and blue arrow is the substrate

the LW-SAW sensors were not working anymore after the deposition of NCD layer. The possible explanation is, that during the diamond deposition, the ZnO layers became conductive by elimination of oxygen disorders, that acts as acceptors and eliminates the free charge in the ZnO layers.

## Conclusions

- Comparison of experimental and theoretical data showed a discrepancy originating from different mechanical properties of SiO<sub>2</sub> and diamond materials used in simulations and in real sensors.
- The simulations were corrected to fit the experimental data giving

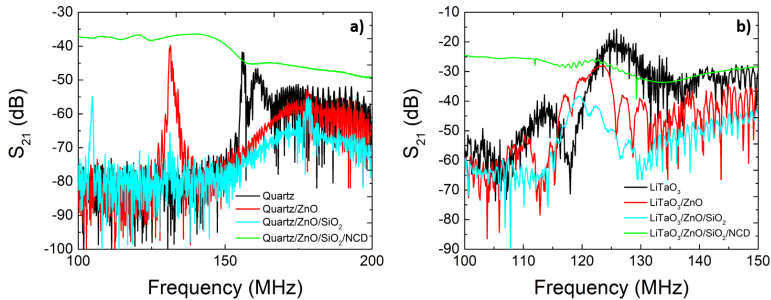


Figure 4.16: Spectra of transmission coefficient  $S_{21}$  for LW-SAW sensors with ZnO layers deposited on a) ST-cut quartz and b)  $36^\circ\text{YX}$   $\text{LiTaO}_3$  substrates,  $\lambda = 32 \mu\text{m}$

the Young modulus equal to 60 GPa and 240 GPa for  $\text{SiO}_2$  and NCD layer respectively. Nanoindentation measurements confirmed such low value of diamond Young modulus.

- This result is important as it shows that the obtained simulation results for diamond coated sensors does not completely reflect their real behavior.
- Expected big drop in sensitivity for diamond coated LW-SAW sensors were not observed. This result is very promising for fabrication of LW-SAW biosensor with integrated diamond layer.
- ZnO layers were successfully coated by NCD layers by using thin  $\text{SiO}_2$  protective layer. Unfortunately, LW-SAW sensors with ZnO guiding layer stopped working after diamond layers deposition.

## 4.5 Bacteriophage's tail fibers production

All of the proteins were obtained during a six months stay at the National Centre of Biotechnology (CNB-CSIC) in Madrid, Spain within the research group Structural Biology of Viral Fibers under the leadership of Mark J. van Raaij.

Production and purification of his-tagged proteins can be divided into four main steps - 1) transformation of the plasmid carrying the genes for the desired protein and also the genes for antibiotic resistance in the suitable bacteria cells, 2) growth of the transformed bacteria cells and protein expression, 3) harvesting of cells, their lysis and collecting the protein and 4) protein purification. Simplified schematic of protein production and purification process is shown in the figure 4.17.

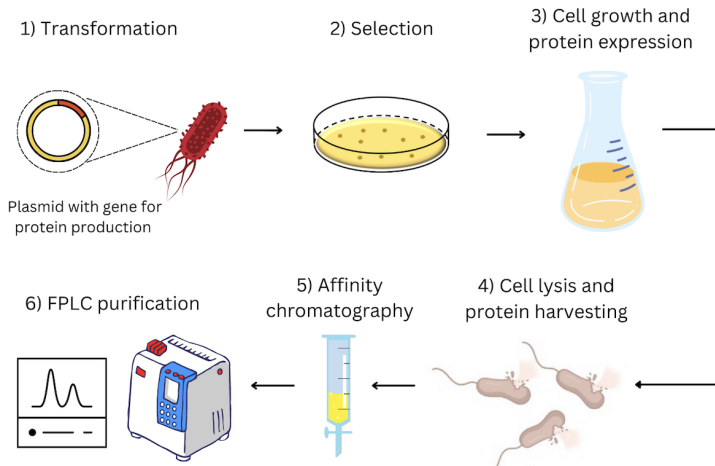


Figure 4.17: Schematic of protein production and purification

Within this work, three different tail fibers were produced - gp17 from bacteriophage T7, gp12 from phage T4 and ORF26 from phage T1. Detailed protein production will not be discussed here and can be found in whole Thesis.

The important aspect of biorecognition element in biosensing is its specificity. The binding of produced protein were tested with three different bacteria strains *Escherichia coli* BL21(DE3-), *Salmonella enterica* subsp. enterica serovar Anatum A1 and *Staphylococcus aureus* RN9220  $\Delta$ SpA. All of them are expected to bind only to *E. coli* cells. Binding were tested by immunofluorescence assay and the read-out were

performed using confocal microscopy. Schematic of the immunofluorescence assay principle is shown in the figure 4.18. Results are shown in the figure 4.19 and listed in the table 4.1.

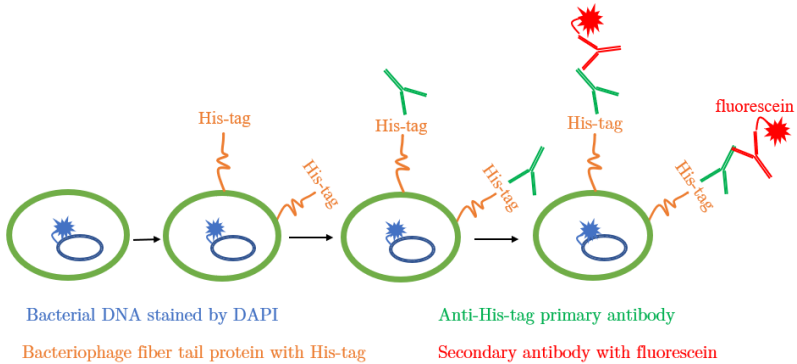


Figure 4.18: Schematic of the immunofluorescence assay

Table 4.1: Expectation and results of protein binding to bacteria cells

	gp17		gp12		ORF26	
	expected	result	expected	result	expected	result
<i>E. coli</i>	✓	✓	✓	✓	✓	✓
<i>Salmonella</i>	×	×	×	✓	×	×
<i>Staphylococcus</i>	×	×	×	×	×	×

## Conclusions

- Three different N-terminally his-tagged bacteriophage's tail fibers proteins binding to *E. coli* were successfully produced.
- Gp17 protein as well as ORF26 bind to *E. coli* cells as was expected, gp12 also binds a little bit to *Salmonella* cells, which can lead to non-specific interactions when used in biosensors.

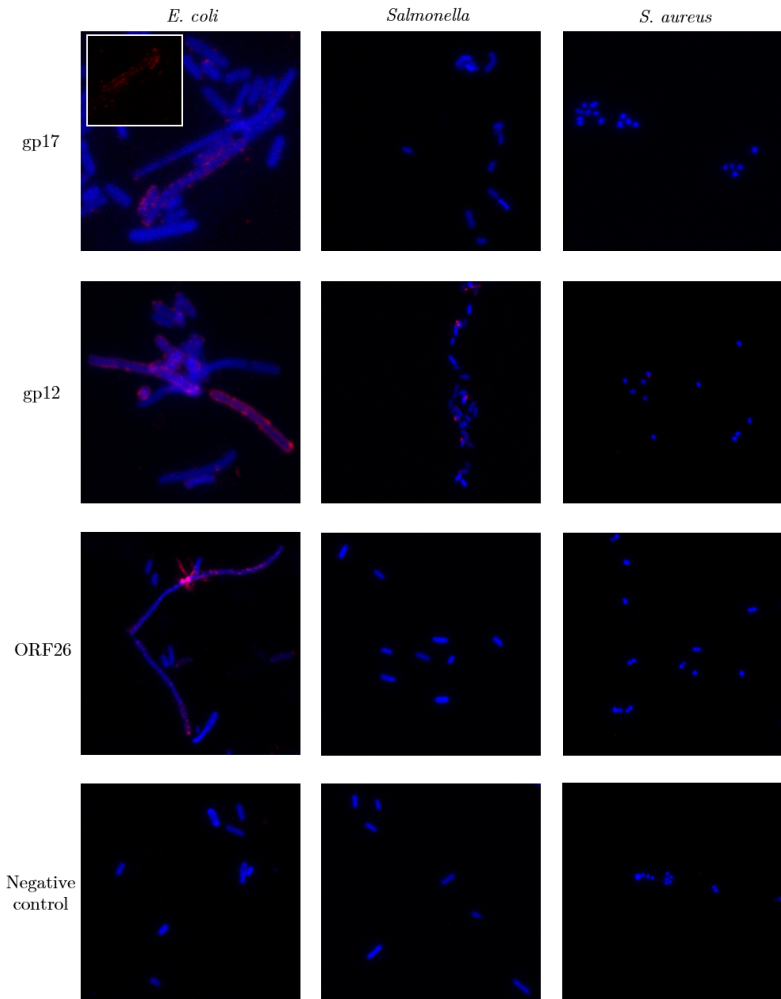


Figure 4.19: Results from bacteria binding study using fluorescent microscopy. Three different strains of bacteria were tested for protein binding. Blue are the bacterial cells stained by DAPI and red are the attached proteins to the bacteria cells.

## 4.6 Functionalization of the diamond layers

For the immobilization of the (His)<sub>6</sub>-tagged proteins, it is necessary to introduce metal cations on the surface. In this work, two different approaches were used to obtain Ni<sup>2+</sup> ions on the BDD surface: 1/ attachment of nitriloacetic acid (NTA), which is one of the most common chelating agent used for immobilization of metal cations and 2/ introduction of nickel nanoparticles (NiNPs) on diamond surface. Both of the functionalization approaches were carried out using electrochemical methods, so the boron-doped diamond (BDD) layers were used.

### 4.6.1 Electrodeposition of nickel nanoparticles

CV measurement in 1 mmol · L<sup>-1</sup> [Fe(CN)<sub>6</sub>]<sup>3-/4-</sup> in 10 mmol · L<sup>-1</sup> PBS (pH 7.4) of sample 1 reveals the reversible redox couple at cca 180 mV/300 mV corresponding to the surface confined Ni(II)/oxyhydroxide species (see graph 4.21). The anodic peak at 300 mV corresponds to the oxidation of Ni(OH)<sub>2</sub> to NiO(OH) and cathodic peak at 180 mV reduction of NiO(OH) back to Ni(OH)<sub>2</sub> [19]. These peaks disappeared after gp17 protein binding, which confirmed that Ni(II)/oxyhydroxide species are involved in the protein's attachment. The characteristic reversible redox peaks of the [Fe(CN)<sub>6</sub>]<sup>3-/4-</sup> decreased after incubation with gp17 protein and *E.coli* cells, that indicates a partial inactivation of the electrode surface resulting from protein and bacteria binding. SEM measurement revealed uniform deposition of spherical NiNPs with an approximate diameter of 200 nm covering the entire working electrode surface, see picture 4.20.

### 4.6.2 Protein attachment via covalent grafting of NTA acid

Functionalization of BDD electrodes by NTA acid was carried out according to procedure described in [20]. Functionalization was done in two steps (electrochemical activation of the surface and attachment of

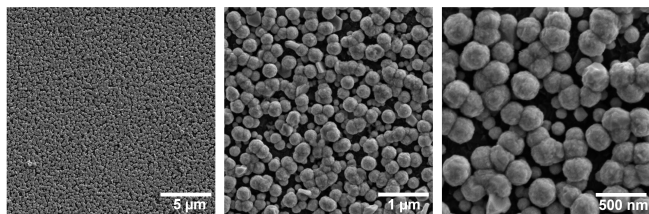


Figure 4.20: Low and high magnification scanning electron micrographs of NiNPs deposited on BDD electrode

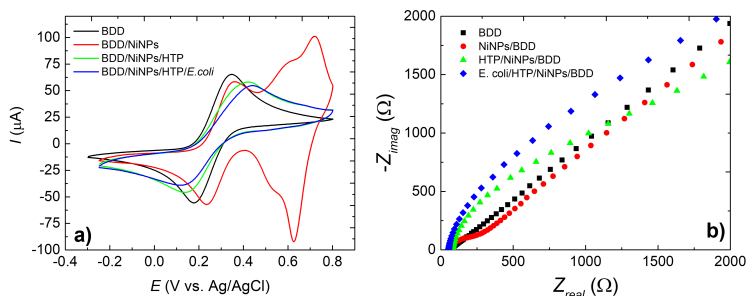


Figure 4.21: a) Cyclic voltammograms of  $1 \text{ mmol} \cdot \text{L}^{-1} [\text{Fe}(\text{CN})_6]^{3- / 4-}$  in  $10 \text{ mmol} \cdot \text{L}^{-1}$  PBS (pH 7.4) and b) Nyquist plot of  $1 \text{ mmol} \cdot \text{L}^{-1} [\text{Fe}(\text{CN})_6]^{3- / 4-}$  in  $1 \text{ mol} \cdot \text{L}^{-1}$  KCl recorded on bare BDD electrode, BDD/NiNPs, BDD/NiNPs/HTP and BDD/NiNPs/HTP/*E.coli*, HTP - his-tagged gp17 protein

NTA acid) followed by (His)6-tagged gp17 protein and *E.coli* bacteria attachment.

As carboxylic groups are protonated in acidic environment, there should be barely no interaction between redox marker and surface electrode in HCl after all modification steps. This is confirmed by CV measurements, see figure 4.22a), when there is small increase in  $\Delta E_p$  values after AB acid and NTA acid attachment steps. In neutral environment (PBS pH 7.4) carboxylic groups are dissociated (negatively charged  $-\text{COO}^-$  groups) which results in electrostatic repulsion of modified electrode's surface and  $[\text{Fe}(\text{CN})_6]^{3- / 4-}$  anions. This can be ob-

served as a significant increase in  $\Delta E_p$  values, which was also confirmed, see figure 4.22b).

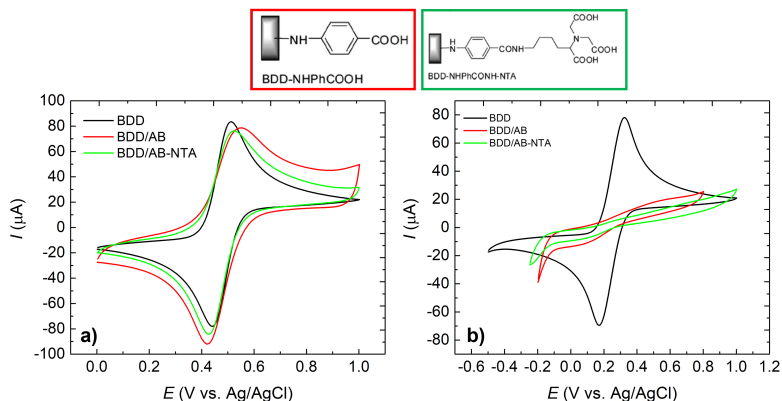


Figure 4.22: Cyclic voltammograms of a)  $1 \text{ mmol} \cdot \text{L}^{-1} [\text{Fe}(\text{CN})_6]^{3-/4-}$  in  $0.5 \text{ mol} \cdot \text{L}^{-1} \text{ HCl}$  (pH 0.3) and b)  $1 \text{ mmol} \cdot \text{L}^{-1} [\text{Fe}(\text{CN})_6]^{3-/4-}$  in  $10 \text{ mmol} \cdot \text{L}^{-1} \text{ PBS}$  (pH 7.4) recorded on bare BDD electrode, BDD/AB-acid, BDD/AB-NTA acid

The electrochemical measurements confirmed the attachment of NTA acid to the BDD electrode's surface, so we proceed to the  $\text{Ni}^{2+}$  incubation followed by 6-his-tagged gp17 protein and *E. coli* cells attachment. After incubation with his-tagged gp17 protein, we can observe appearance of the peaks, which could indicate attachment of the his-tagged protein via  $\text{Ni}^{2+}$  ions to the NTA acid on the BDD surface, see graph 4.23a). We could observe appearance of the peaks in the CV spectra after *E. coli* attachment, which indicates that the attachment was not successful. To exclude non-specific interaction of the bacteria, we also incubated bare BDD electrode with the bacteria culture. CV measurement indicated, that there is no attachment of bacteria cells to the non-modified BDD electrode, see graph 4.23b).

To confirm the results of CV measurement, sample 6 was kept in 10 % formaldehyde in DI water overnight at  $4 \text{ }^\circ\text{C}$  to fix the bacteria and AFM was measured. As a control, *E.coli* culture was dropped also on the bare glass substrate and fixed *E* in the same way as on BDD

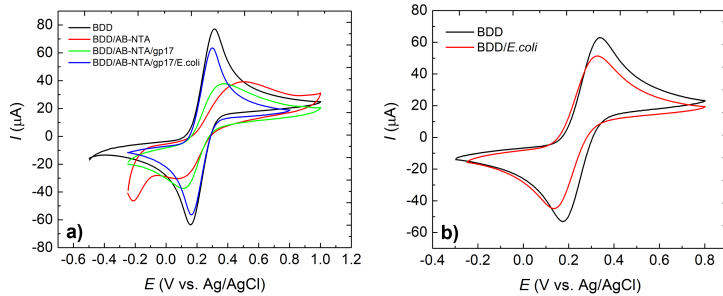


Figure 4.23: Cyclic voltammograms of  $1 \text{ mmol} \cdot \text{L}^{-1} [\text{Fe}(\text{CN})_6]^{3-/4-}$  in  $10 \text{ mmol} \cdot \text{L}^{-1}$  PBS (pH 7.4) recorded a) on bare BDD electrode, BDD/AB-NTA acid, BDD/AB-NTA/*his*-tagged gp17 protein and BDD/AB-NTA/gp17/*E.coli* and b) on bare BDD electrode and BDD/*E.coli* electrode

electrode. The bacteria were not found on the surface of modified BDD electrode, but were clearly visible on the glass substrate, see picture 4.24.

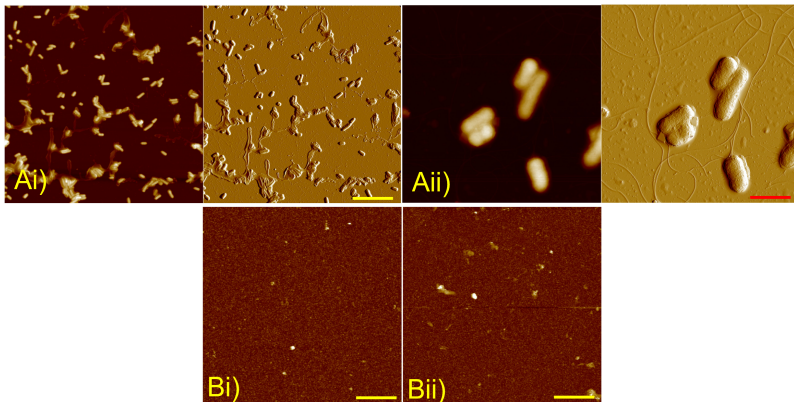


Figure 4.24: AFM micrographs of *E.coli* cells on the A) glass substrate and B) functionalized BDD electrode, yellow bar indicates  $8 \mu\text{m}$  and red bar  $1 \mu\text{m}$

## Conclusions

- Two different approaches for attachment of his-tagged proteins were successfully tested.
- According to CV measurement, bacteria were successfully attached to the functionalized BDD surface using NiNPs protocols, but their attachment using NTA acid approach was not successful. Unfortunately, AFM measurement did not confirm successful attachment of *E. coli* cells to the BDD surface.

## 4.7 BDD-coated QCM sensors for biosensing

Piezoelectric Quartz Crystal Microbalance (QCM) sensors are cheap, mass-produced bulk acoustic sensors. Their mass sensing capabilities can be combined with electrochemical detection in so-called electrochemical quartz crystal microbalance (EQCM).

QCM crystals with working frequency at 10 MHz were purchased from company Krystaly, Hradec Králové a.s. BDD layers were deposited on the gold electrode at low temperature by procedure described in Methods.

### Sensitivity study

To investigate QCMs performance in liquid, solutions with 3 different sucrose weight percent 7.5 %, 15 % and 30 % were used. QCMs sensors behavior in liquid with different viscosity and density is not affected by adding the BDD coating, as the frequency shift was linearly proportional to the sucrose weight concentration and comparable for all BDD-coated QCMs and uncoated QCM sensor, see graph 4.25a).

The sensor's sensitivity was investigated using gold nanoparticles (AuNPs) solutions. 3 consecutive measurements were done by dropping 10  $\mu$ l of AuNPs solution on the QCM sensor surface, letting the liquid dry and the frequency variation was then measured. Plain QCM sensor showed higher relative frequency shift (-0.04 % for 30  $\mu$ l of AuNPs) in

comparison to BDD-coated QCM sensors ( $-0.027\%$ ) for both BDD layer thicknesses (130 and 320 nm), see graph 4.25b). This experiment showed decrease in sensitivity after adding BDD layer on QCM sensor, but the sensitivity is not affected by thickness of the added BDD layer.

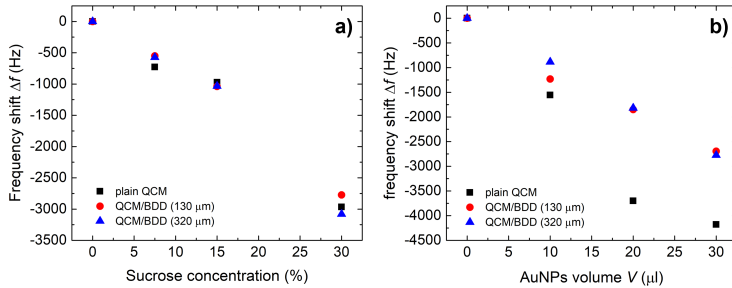


Figure 4.25: Frequency shift of plain and BDD-coated QCM sensor in a) solutions with different sucrose concentrations and b) different volume of AuNPs solutions

### BDD/QCM surface functionalization

Both previously described approaches were tested, when attachment of NiNPs were tested at first.

CV measurement in  $1 \text{ mmol} \cdot \text{L}^{-1}$   $[\text{Fe}(\text{CN})_6]^{3-/4-}$  in  $10 \text{ mmol} \cdot \text{L}^{-1}$  PBS (pH 7.4) electrolyte reveals the reversible redox couple corresponding to the surface confined Ni(II)/oxyhydroxide species, that confirms successful electrodeposition of NiNPs, see graph 4.26a). CVs were also measured in the 1 M KCl that provides signal directly from deposited NiNPs, where we can observe significant reduction of the signal from NiNPs after incubation with his-tagged protein, which indicates attachment of the protein to the NiNPs, see graph 4.26b).

QCM sensors were also frequency characterized before and after deposition of NiNPs. As the functionalized QCM sensor are intended to be used in biosensing, they were also characterized in PBS buffer. Characterization was carried out using OpenQCM  $Q^{-1}$  device. Funda-

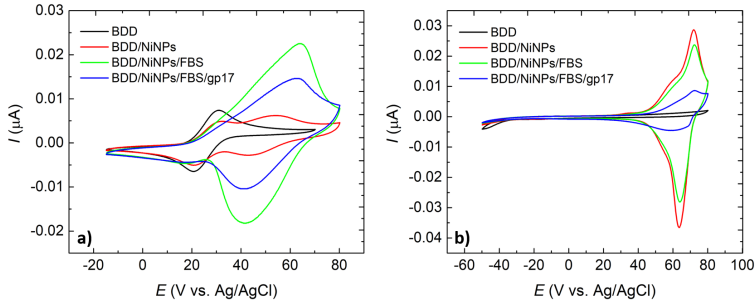


Figure 4.26: Cyclic voltammograms of a)  $1 \text{ mmol}\cdot\text{L}^{-1} [\text{Fe}(\text{CN})_6]^{3-}/4-$  in  $10 \text{ mmol}\cdot\text{L}^{-1}$  PBS (pH 7.4) and b)  $1 \text{ M KCl}$  recorded on bare BDD electrode, BDD/NiNPs and DD/NiNPs/FBS and BDD/NiNPs/FBS/HTP

mental frequency of QCMs was measured on air or by adding of  $200 \mu\text{l}$  of PBS buffer.

Table 4.2: Relative frequency shift of QCMs before and after NiNPs deposition on air and in PBS buffer

Electrode number	1	2	3
$f_0$ (Hz)	9998000	9975274	9973912
$\Delta f$ in PBS (%)	-0.0592	-0.0566	-0.06018
$\Delta f$ NiNPs on air (%)	-0.0328	-0.0463	-0.0282
$\Delta f$ NiNPs in PBS (%)	-0.0419	-0.0521	-0.0548
$\Delta f$ NiNPs on air after PBS (%)	<b>0.0259</b>	-0.0194	<b>0.0205</b>

It is expected, that frequency shift in PBS will be higher than in the air. Also is expected negative frequency shift after deposition of NiNPs due to mass loading on the surface. This is fulfilled for both measurements in PBS (before and after NiNPs deposition) and for QCM's with NiNPs on air. But we can observe positive frequency increment after QCM's with NiNPs in PBS buffer, in table 4.2 are highlighted in red color, which means, that NiNPs are not attached well to the sensor's surface and they are washed away during the frequency measurement, probably due to the vibrations of the sensor.

Attachment of the NTA acid to the BDD coated QCM sensor was not achieved so far.

### Conclusions

- Deposition of BDD layers on QCM sensors was successfully achieved.
- The study of the influence of adding the BDD layer did not show any significant change in the behavior of QCM sensors in liquid with different density and viscosity. QCM's sensitivity slightly decreased after adding BDD layer in comparison with plain QCM sensor.
- Two different E/C functionalization protocols were studied in order to attach his-tagged gp17 protein to BDD layers. According to CV results, the deposition of NiNPs followed by attachment of gp17 protein was successfully achieved.
- NiNPs were washed away during the frequency characterization of QCM sensors in PBS buffer.
- The second approach, electrografting of NTA acid to BDD layer, was not achieved so far on QCM sensors.

## 5 | List of publications

### Publications related to the doctoral thesis topic

- Talbi A., Soltani A., Rumeau A., Taylor A., **Drbohlavova L.**, Klimsa L., Kopecek J., Fekete L., Krecmarova M., Mortet V.: Simulations, fabrication and characterization of diamond-coated Love wave-type surface acoustic wave sensors. *Physica status solidi (a)* 2015, **212(11)**, 2606-2610, IF = 2.17
- **Drbohlavova L.**, Bulir J., Vales V., Krecmarova M., Taylor A., Talbi A., Soltani A., Mortet V.: Fabrication methods of diamond coated Love wave SAW biosensors for bacterial detection applications. In *Instruments and Methods for Biology and Medicine 2015*. Kladno: Czech Technical University in Prague, 2015, p. 18-23. ISBN 978-80-01-05851-0
- **Drbohlavova L.**, Gerbedoen J.C., Taylor A., Talbi A., Fekete L., Ashcheulov P., Soltani A., Bovtun V., Kempa M., Bartoň J., Cigler P., Mortet V.: Diamond Coated LW-SAW Sensors-Study of Diamond Thickness Effect. *MDPI Proceedings* **2017**, 1, 540, ISSN 2504-3900
- Liu Y., Talbi A., Djafari-Rouhani B., El Boudoti E. H., **Drbohlavová L.**, Mortet V., Bou Matar O., Pernod P. Interaction of Love waves with coupled cavity modes in a 2D holey phononic crystal. *Physics Letters A* 2019, **383(13)**, 1502-1505 DOI: 10.1016/j.physleta.2019.01.053. ISSN 03759601, IF = 2.707
- **Drbohlavová L.**, Fekete L., Bovtun V., Kempa M., Taylor A., Liu Y., Bou Matar O., Talbi A., Mortet V. Love-wave devices with continuous and discrete nanocrystalline diamond coating for biosensing applications. *Sensors and Actuators A: Physical*. 2019, 298. DOI: 10.1016/j.sna.2019.111584. ISSN 09244247, IF = 4.291

### Publications not related to the doctoral thesis topic

- Mortet V., **Drbohlavová L.**, Lambert N., Taylor A., Ashcheulov P., Davydova M., Lorincik J., Aleshin M., Hubik P., Conductivity

---

of boron-doped diamond at high electrical field. *Diamond and Related Materials* 2019, **98** DOI: 10.1016/j.diamond.2019.107476. ISSN 09259635, IF = 4.1

## **Participation to international conferences**

### **Oral presentation**

- “Fabrication methods of diamond coated Love wave SAW biosensors for bacterial detection applications”, Instruments & Methods for Biology and Medicine 2015 (IMBM 2015) student conference, FBME CTU in Prague, Sitna Sq. 3105, Kladno Czech Republic May 28<sup>th</sup>, 2015

### **Poster presentation**

- “Simulations, fabrication and characterizations of diamond coated Love wave surface acoustic wave sensors” at Hasselt Diamond workshop 2015 - SBDD XX, Cultureel centrum Hasselt, Hasselt, Belgium, February 25<sup>th</sup> - 27<sup>th</sup>, 2015
- “Love-wave type surface acoustic wave sensors: effect of diamond thin film coating thickness” at Hasselt Diamond workshop 2017 – SBDD XXII, Cultureel centrum Hasselt, Hasselt, Belgium, March 8<sup>th</sup>-10<sup>th</sup>, 2017
- "Diamond Coated LW-SAW Sensors-Study of Diamond Thickness Effect" at Eurosensors 2017, Paris, France, September 3<sup>th</sup> - 6<sup>th</sup>, 2017
- “Theoretical investigation of diamond coated SiO<sub>2</sub>/ST-quartz and SiO<sub>2</sub>/36°YX LiNbO<sub>3</sub> structures for biosensing applications” at E-MRS Fall meeting 2018, Warsaw, Poland, September 17<sup>th</sup> – 20<sup>th</sup>, 2018
- "Diamond and silicon carbide as passivation layers for packageless SAW sensors" at MRS Virtual Spring/Fall meeting Boston 2020, November 27<sup>th</sup> - December 4<sup>th</sup>, 2020
- "Enhancing the sensitivity of SAW sensors using the diamond surface phononic metamaterials" at MRS Virtual Spring/Fall meeting Boston 2020, November 27<sup>th</sup> - December 4<sup>th</sup>, 2020

# Bibliography

- [1] Asif Ahmed, Jo V. Rushworth, Natalie A. Hirst, and Paul A. Millner. Biosensors for whole-cell bacterial detection. *Clinical Microbiology Reviews*, 27:631–646, 2014.
- [2] Robert S. Burlage and Joshua Tillmann. Biosensors of bacterial cells. *Journal of Microbiological Methods*, 138:2–11, 2017.
- [3] Hüseyin Oğuzhan Kaya, Arif E. Cetin, Mostafa Azimzadeh, and Seda Nur Topkaya. Pathogen detection with electrochemical biosensors: Advantages, challenges and future perspectives, 2 2021.
- [4] Jordi Riu and Barbara Giussani. Electrochemical biosensors for the detection of pathogenic bacteria in food, 5 2020.
- [5] Nishant Kumar, Yuan Hu, Suman Singh, and Boris Mizaikoff. Emerging biosensor platforms for the assessment of water-borne pathogens. *The Analyst*, 143:359–373, 2018.
- [6] Dmitri Ivnitcki, Ihab Abdel-Hamid, Plamen Atanasov, Ebtisam Wilkins, and Stephen Stricker. Application of electrochemical biosensors for detection of food pathogenic bacteria. *Electroanalysis*, 12:317–325, 3 2000.
- [7] M. B. Maas, W. J. Perold, and L. M.T. Dicks. Biosensors for the detection of escherichia coli, 10 2017.
- [8] J Du, G.L Harding, A.F Collings, and P.R Dencher. An experimental study of love-wave acoustic sensors operating in liquids. *Sensors and Actuators A: Physical*, 60:54–61, 5 1997.
- [9] V. Vaijyanthimala, Po Yun Cheng, Shih Hua Yeh, Kuang Kai Liu, Cheng Hsiang Hsiao, Jui I. Chao, and Huan Cheng Chang. The long-term stability and biocompatibility of fluorescent nanodiamond as an in vivo contrast agent. *Biomaterials*, 33:7794–7802, 2012.
- [10] Anke Krueger and Daniel Lang. Functionality is key: Recent progress in the surface modification of nanodiamond. *Advanced Functional Materials*, 22:890–906, 3 2012.
- [11] Vadym N. Mochalin, Olga Shenderova, Dean Ho, and Yury Gogotsi. The properties and applications of nanodiamonds, 2012.
- [12] K. Nakamura, M. Kazumi, and H. Shimizu. Sh-type and rayleigh-type surface waves on rotated y-cut litao3. pages 819–822. IEEE, 1977.
- [13] María Isabel Rocha Gaso. Analysis, implementation and validation of a love mode surface acoustic wave device for its application as sensor of biological processes in liquid media., 2013.

- [14] Zhenwei Peng and Simon A.T. Redfern. Mechanical properties of quartz at the alpha-beta phase transition: Implications for tectonic and seismic anomalies. *Geochemistry, Geophysics, Geosystems*, 14:18–28, 1 2013.
- [15] H. J. Levinstein, A. A. Ballman, and C. D. Capio. Domain structure and curie temperature of single-crystal lithium tantalate. *Journal of Applied Physics*, 37:4585–4586, 11 1966.
- [16] G. A. Smolenskii, N. N. Krainik, N. P. Khuchua, V. V. Zhdanova, and I. E. Mylnikova. The curie temperature of linbo3. *Physica status solidi b*, 13:309–314, 1966.
- [17] L. Drbohlavová, L. Fekete, V. Bovtun, M. Kempa, A. Taylor, Y. Liu, O. Bou Matar, A. Talbi, and V. Mortet. Love-wave devices with continuous and discrete nanocrystalline diamond coating for biosensing applications. *Sensors and Actuators, A: Physical*, 298, 2019.
- [18] A. Taylor, L. Klimša, J. Kopeček, Z. Remeš, M. Vronka, R. Čtvertlík, J. Tomáščík, and V. Mortet. Synthesis and properties of diamond - silicon carbide composite layers. *Journal of Alloys and Compounds*, 800:327–333, 2019.
- [19] Mallikarjunarao Ganesana, Georges Istarnboulie, Jean louis Marty, Thierry Noguer, and Silvana Andreescu. Site-specific immobilization of a ( his ) 6-tagged acetylcholinesterase on nickel nanoparticles for highly sensitive toxicity biosensors. *Biosensors and Bioelectronics*, 30:43–48, 2011.
- [20] Quang Thuan Tran, Jacques De Sanoit, Sylvie Pierre, Jean Charles Arnault, and Philippe Bergonzo. Diamond electrodes for trace alpha pollutant sequestration via covalent grafting of nitrilotriacetic acid (nta) ligand. *Electrochimica Acta*, 136:430–434, 2014.
- [21] O. A. Williams, A. Kriele, J. Hees, M. Wolfer, W. Müller-Sebert, and C. E. Nebel. High young's modulus in ultra thin nanocrystalline diamond. *Chemical Physics Letters*, 495:84–89, 7 2010.

## 6 | Summary

The work presented here is the first step towards the development of Love-wave biosensors with integrated diamond layer. FEM simulations of diamond coated LW-SAW sensors were performed to study the effect of diamond layer on the sensors' behavior. The observed sensitivity decrease after the diamond layer addition was a building stone for further chapters focusing on the experimental comparison of LW-SAW sensors with continuous diamond layer or discrete diamond coating or theoretical investigation of the integration of LW-SAW sensors with phononic metamaterials.

The experimental investigation of diamond-coated LW-SAW sensors brought an discrepancy with the theoretical results as we did not observe such big sensitivity drop in real diamond-coated sensors as expected from simulations. We found out, that the mechanical properties of NCD layer are different than we used in simulations. Mainly Young's modulus has much lower values  $\sim 240$  GPa in comparison with 1050 GPa used in simulations.

Three different his-tagged bacteriophage tail fibers were produced and purified in order to attach them to the diamond layer as a bioreceptor. Two different protocols were successfully implemented to attach the proteins to the BDD layers.

The large amount of work carried out in this Thesis demonstrates that the development of diamond-based acoustic biosensor is complex task. In contrary to previous publication [21], we found out late that the mechanical properties of simulated NCD layers and the layers deposited at low temperature are different. This result drastically changes the perspectives of diamond use in acoustic devices. Diamond-coated LW-SAW sensors are still good candidates to develop sensitive real-time device for bacteria detection in liquids. As the BDD layers are very good electrochemical electrodes with excellent properties and the routes for their electrochemical functionalization are known, it will be advantageous to connect two different signal read-outs at one devices - electrochemical and acoustic characterization, either in LW-SAW sensors or QCM devices respectively.

## 7 | Resumé

Zde prezentovaná práce je prvním krokem k vývoji Love-wave biosenzorů s integrovanou diamantovou vrstvou. FEM simulace diamantem potažených LW-SAW senzorů byly provedeny pro studium vlivu diamantové vrstvy na chování senzorů. Pozorovaný pokles citlivosti po přidání diamantové vrstvy byl stavebním kamenem pro další kapitoly zaměřené na experimentální srovnání LW-SAW senzorů s kontinuální diamantovou vrstvou nebo diskretním diamantovým povlakem nebo teoretickou studií integrace LW-SAW senzorů s fononickými metamateriály.

Experimentální studie LW-SAW senzorů s diamantovou vrstvou přineslo rozpor s teoretickými výsledky, protože u skutečných senzorů s diamantovou vrstvou jsme nezaznamenali tak velký pokles citlivosti, jak se očekávalo ze simulací. Zjistili jsme, že mechanické vlastnosti NCD vrstvy jsou jiné, než jaké jsme použili v simulacích. Především Youngův modul má mnohem nižší hodnoty  $\sim 240$  GPa ve srovnání s 1050 GPa používanými v simulacích.

Tři různé baktériofágové proteiny s his-tag značkou byli vyrobeny a purifikovány, aby mohli být použité jako bioreceptor. Dva různé protokoly byly úspěšně implementovány pro navázání proteinů k povrchu BDD vrstev.

Velké množství práce odvedené v této práci ukazuje, že vývoj akustického biosenzoru na bázi diamantu je složitý úkol. Na rozdíl od předchozí publikace [21] jsme pozdě zjistili, že mechanické vlastnosti simulovaných NCD vrstev a vrstev nanesených při nízké teplotě jsou odlišné. Tento výsledek drasticky mění perspektivy použití diamantu v akustických zařízeních. Snímače LW-SAW s diamantovou vrstvou jsou stále dobrými kandidáty na vývoj citlivého zařízení pro detekci bakterií v kapalinách v reálném čase. Protože vrstvy BDD jsou velmi dobré elektrochemické elektrody s vynikajícími vlastnostmi a způsoby pro jejich elektrochemickou funkcionalizaci jsou známy, bude výhodné propojit dva různé snímače signálu na jednom zařízení - elektrochemickou a akustickou charakterizaci, buď v senzorech LW-SAW, popř. QCM senzorech.